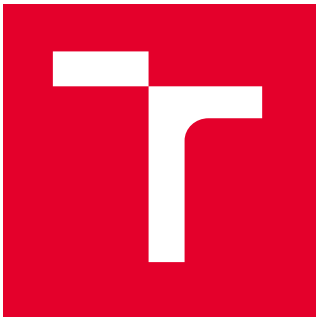

BRNO UNIVERSITY OF TECHNOLOGY

VYSOKÉ UČENÍ TECHNICKÉ V BRNĚ

FACULTY OF MECHANICAL ENGINEERING

FAKULTA STROJNÍHO INŽENÝRSTVÍ

INSTITUTE OF MATERIALS SCIENCE AND ENGINEERING

ÚSTAV MATERIÁLOVÝCH VĚD A INŽENÝRSTVÍ

INTERACTION OF PULSATING WATER JET WITH SURFACE OF STRUCTURAL MATERIALS

INTERAKCE PULSUJÍCÍHO VODNÍHO SVAZKU S POVRCHEM KONSTRUKČNÍCH MATERIÁLŮ

DOCTORAL THESIS

DIZERTAČNÍ PRÁCE

AUTHOR — **Ing. Jakub Poloprudský**

AUTOR PRÁCE

SUPERVISOR — **prof. Mgr. Tomáš Kruml, CSc.**

ŠKOLITEL

BRNO 2024

Abstract

The pulsating water jet (PWJ) is a hybrid technological modification of the continuous water jet (CWJ) working at the principle of impact pressure. PWJ is created by splitting the coherent stream of water into discrete clusters. The clusters create the so-called water hammer effect, which significantly increases the effectivity of erosion of the material subjected to PWJ. This work deals with the interaction of water clusters created by the PWJ with the surface of selected structural material. The work focuses on the incubation erosion stage before the start of the material removal. The experimental material used was austenitic 316L stainless steel due to the excellent corrosion resistance in tap water environment and structural homogeneity. the material is according to literature review common for waterjet focused research. The PWJ is a novel technology with several technological parameters, which offers the potential for technology optimization and opens questions about its possibilities and limitations. The individual clusters of water are expected to act upon the surface in a similar way as liquid droplets. Under this approximation, the technology is currently a candidate for use as an erosion testing tool. The advantages of PWJ erosion testing compared to conventional erosion testing tools are the high frequency of impacts and control over the impact speed, droplet size, angle of droplet impacts and impact frequency.

The work focuses on the incubation erosion stage, which is the stage prior to macroscopic material removal. The incubation stages consist of plastic deformation of the material, surface deformation exposing the grain boundaries and the creation of surface steps. The goal is to tune the use of PWJ technology for erosion testing, surface roughening and surface strengthening. The main findings are as follows:

- 316L stainless steel was treated with PWJ moving along a linear trajectory with different levels of pressure and cluster impact distribution. The influence of cluster impact distribution on the erosion stage was evaluated.
- The static PWJ with increasing erosion time was done on 316L steel. The subsurface changes corresponding with surface changes were documented using transmission electron microscopy. A new erosion stage was proposed between material roughening and macroscopic material removal stages. This stage precedes the formation of micropits and is defined by the presence of cracks at preferential sites.
- The surface hardening of 316L steel was measured on cross-sections after PWJ treatment. Hardening up to depth of 100 μm was observed before significant material removal started.
- A substantial increase of the fatigue life of 316L steel specimen after treatment by PWJ was found. This is a quite interesting and original finding, opening the possibility of developing a new way for surface engineering. The dependence between PWJ the feed rate and a number of cycles to failure was measured for two strain levels within the experimental design.
- Electron back scattered diffraction measurement was done before and after PWJ treatment. Changes in grain orientation were measured and kernel average misorientation was evaluated. The proposal of this new methodology for erosion incubation stage observation is the highlight of this work.

Keywords: Erosion, Wear, Plastic deformation, Water cluster, Pulsating water jet, Surface hardening, Surface roughening

Abstrakt

Pulzní vodní svazek je modifikace konvenčního kontinuálního vodního svazku. Principem technologie je vyvolání rozpadu koherentního vodního proudu na jednotlivé shluky vodních kapek. Shluky působí v momentě dopadu na povrch impaktním tlakem, což významně zvedá erozní vlastnosti proudu. Práce studuje interakci pulzního vodního svazku s povrchem konstrukčních materiálů. Práce se zaměřuje zejména na inkubační erozní etapa. Inkubační erozní etapa se projevuje plastickou deformací povrchu bez přítomnosti makroskopického úběru materiálu. austenitické korozivzdorná ocel 316L byla zvolena jako experimentální materiál. Pulzující vodní proud je poměrně nová technologie s množstvím propojených technologických parametrů. Množství parametrů poskytuje velký prostor pro optimalizaci technologie v závislosti na použití. Předpokládá se, že vodní shluky svazku působí na povrch podobně jako vodní kapky. Na základě tohoto zjednodušení se nabízí použití technologie na testování erozní odolnosti materiálů. Výhoda technologie oproti konvenčním metodám testování eroze je vysoká frekvence dopadu kapek až 40 kHz a možnost kontrolovat rychlost, velikost, úhel a frekvenci dopadajících kapek.

Zaměřením práce je zkoumání inkubačního erozního stádia předcházejícího úběru materiálu. Eroze se v tomto stádiu projevuje zdrsňováním povrchu v důsledku plastické deformace materiálu, deformací zrn vedoucímu k odhalování hranic zrn a vytváření povrchového reliéfu uvnitř zrn. Cílem práce je naladění a porozumění fungování pulzního vodního svazku a možné použití technologie pro erozní testování, zdrsňování a zpevňování povrchu. Hlavní dosažená zjištění jsou následující:

- Závislost změny distribuce dopadů vodních kapek s několika úrovněmi hydraulických parametrů byla pozorována na austenitické oceli 316L. Závislost distribuce dopadů vodních kapek na erozní efektivitu a erozní stádium byla popsána.
- Statické erozní testy byly provedeny na oceli 316L. Byly měřeny změny profilu způsobené interakcí s PWJ Podpovrchové změny korespondující se změnami povrchovými byli pozorovány pomocí transmisního elektronového mikroskopu. Bylo definováno erozní stádium mezi zdrsňováním povrchu a makroskopickým úběrem materiálu. Definováno bylo přítomností nespojitých mikro trhlin koncentrujících se zejména na hranicích zrn.
- Zpevňování povrchu oceli 316L bylo měřeno na řezu kolmém k ovlivněnému povrchu. Zpevnění bylo pozorované až do hloubky 100 μm, a předcházelo makroskopickému úběru materiálu.
- Nárůst únavové životnosti oceli 316L byl změřen po zpracování povrchu pomocí pulzujícího vodního svazku. V rámci zvolených experimentálních parametrů byla pozorována závislost rychlosti přejezdu pulzujícího vodního svazku a počtu cyklů do lomu pro dvě zkoumané úrovně řízené celkové deformace.
- Metodologie měření pomocí difrakce zpětně odražených elektronů před a po zpracování povrchu oceli 316L pulzním vodním svazkem byla použita. Metodologie umožňuje měřit vývoj změn v orientaci a deformace uvnitř konkrétních zrn. Otestování metodologie je hlavní příspěvek této práce.

Klíčová slova: Eroze, Opotřebení, Plastická deformace, Kapka vody, Pulzující vodní svazek, Zpevňování povrchu, Zdrsňování

Contents

1. Introduction

The interaction of liquid droplets with the surface of structural materials leads to the start of the erosion process that changes surface properties of the materials. Droplet erosion is considered as a phenomenon which decreases the service life of engineering components such as wind turbine blades [1, 2], steam turbine blades [3], aircraft leading edges [4], steam pipes in nuclear power plants [5–7], etc. These surface changes caused by repeated water droplet impingement can lead to material loss and cause potential failures, but as shown in this work, when applied in a controlled manner they can become effective way of targeted surface disintegration or modification.

The droplet erosion is exploited in this work by using pulsating water jet (PWJ). A device that creates repeated droplet impingement on the surface by splitting continuous water jet into discrete clusters. The discrete clusters then create repeated impact pressure on the surface of treated material. The impact pressure caused by clusters is significantly higher than the Bernoulli stagnation pressure. Controlling the parameters of pulsating water jet and therefore water clusters speed, the interaction can lead to surface roughening or hardening. Both hardening and roughening can be used to create functional surfaces. The hardening can be used for a treatment of welds [8], 3D printed materials or increasing of fatigue life of components.

The experimental part of this work is divided into two experimental sets:

Experimental set 1

- Parametric optimization - One of the main intricacies of the technology is the dependence of standoff distance (distance between the nozzle and material´s surface) on hydraulic parameters of the process. The first experimental part of this work focuses on tuning the standoff distance for austenitic steel 316L

Experimental set 2

- Improving the fatigue life - Based on the knowledge of erosion stages, the PWJ treatment of 316L steel fatigue samples was done with the aim to strengthen the surface and thus enhance the fatigue life of the material. It was shown that the experiment with the increasing number of impingement/mm led to a systematic increase in fatigue life. It is proposed that such treatment can be an alternative to the shot peening procedure.
- Time exposure experiment - Surface was treated by PWJ with exposure time ranging from incubation erosion period to stages of material removal. In this work the focus is on early erosion stages that can be used for surface modification. The surface modifications can be based on surface hardening or surface roughening.
- Incubation erosion stage measurement-The time exposure experiment was repeated only within the incubation interval. Since most of the works evaluate incubation only by surface profilometry, method for surface layer deformation is proposed. The method uses electron back scatter diffraction (EBSD) measurement before and after PWJ exposure on the same marked spot. This allows qualificative observation of changes in grain orientation and misorientation inside the grains. The EBSD measurement can be evaluated statistically to gain quantitative information about eroded areas.

2. Theoretical part

The transient pressure created at the exact moment of impact of the liquid droplet on the the surface is significantly higher than the Bernoulli stagnation pressure. One of the first calculations of this impact pressure was proposed by Cook [9], this phenomenon is called the water hammer effect. Cook defined the water hammer effect as follows: "The pressure generated on an element of the surface at its first encounter with water moving at finite velocity is different from that produced by the steady impact of a moving stream of water at the same velocity" [9]. When the moving column of water is abruptly stopped by a fixed surface, there is a sudden break of the front layer of the water column. If no layer of gas to cushion the blow is present, the velocity energy of the front of the column is transformed into the potential energy of the impact. The generated pressure is only limited by the slight compressibility of the impacted solid and the liquid medium [9]. The water hammer pressure can be expressed as a means of the velocity of the compression wave [10] by Eq. (1):

$$p_{WH} = \rho C v \tag{1}$$

where C is the velocity of the compression wave in the liquid, v is velocity of the water droplet and ρ is the liquid density. When the velocity wave reaches the edge of the droplet before solid surface, the lateral outflow begins. The pressure falls to Bernoulli stagnation pressure calculated [11] by Eq. (2).

$$p_S = \frac{1}{2}\rho v^2 \tag{2}$$

When the continuous stream hits the solid surface, the stagnation pressure (p_S) applies [11].The schematic of pressure development for water column compared to repeated droplet impingement is shown in **Figure 1**.

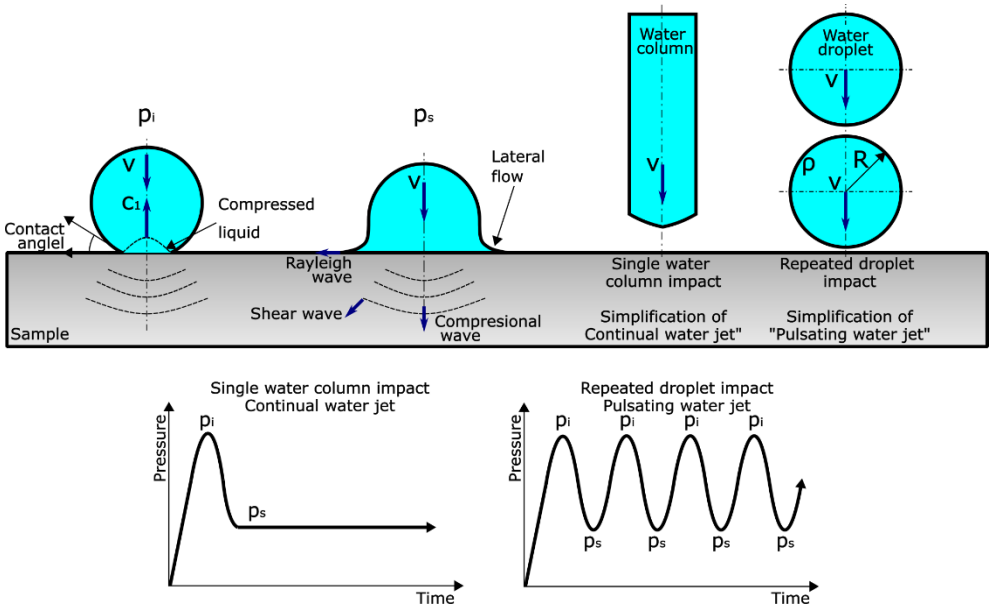

Figure 1 Droplet impingement comparison to water column impingement

The first stage, known as the initial compressible stage, is the transient time when the droplet first hits the solid surface and behaves in a compressible manner [12]. The region of the compressed liquid is on the interface between solid and liquid. The compression is caused by the expansion of the contact periphery between liquid and solid which is faster than the motion

of the shock front. This creates high pressure on the impacted surface of the solid most referred to as water-hammer pressure.

The second stage called lateral outflow begins when the shock front reaches the edge of the solid/liquid interface. At this point, the release of compressed liquid starts. The release causes the high-velocity flow of liquid in the radial direction. The velocity of lateral flow is significantly higher than flow velocity in the impinging direction. This can cause the material removal of uneven surfaces [13]. After the initial effects are depleted the Bernoulli stagnation pressure takes place [14]. These two transient effects are the cause of four general erosion mechanisms of water droplet impingement of solid surfaces: 1) Impact pressure 2) Stress wave propagation 3) The lateral outflow jetting and 4) Hydraulic penetration [14]. The lateral outflow jetting and hydraulic penetration modes require the presence of pre-existing cracks or surface irregularities. This means, that on flat polished material surfaces direct deformation and stress wave propagation are the most contributing effects [14].

The three erosion stages were defined based on the erosion curve of different metallic materials [15]. Stage I-**incubation period** corresponds to a period with no erosion in sense of material loss, but the material is subjected to macroscopic plastic deformation. During the second stage (stage II-**the maximum rate of erosion**), the material removal rate rises to a maximum and then remains constant for a certain period. This stage is characterized by the formation and merging of the erosion pits in the impacted area due to material removal. The third stage (stage III-**the final steady state**) begins when most of the pits across the impacted area are merged to form a single erosion crater or kerf. [15].

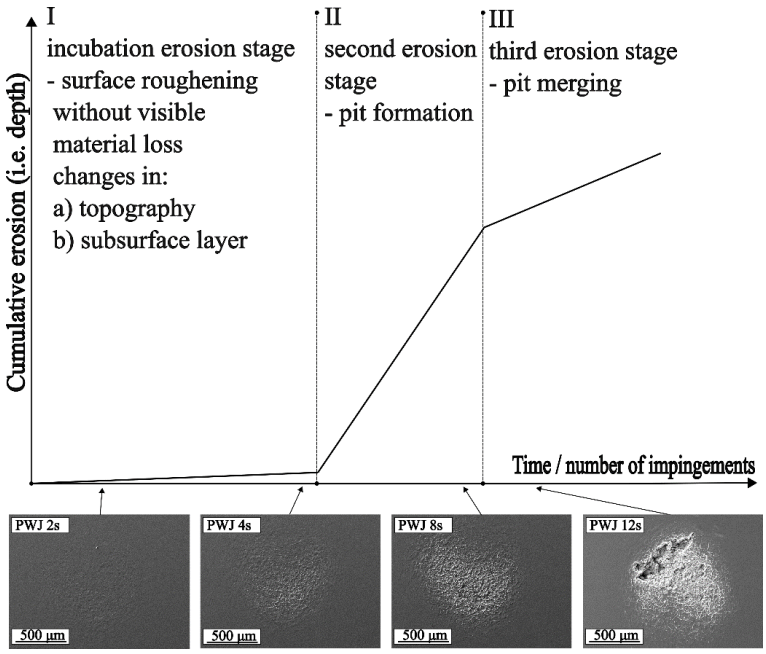

Figure 2 Theoretical erosion curve drawn according to [21] with added examples of eroded surfaces

The erosion potential of repeated water droplet impingement was utilized using Pulsating water jet (PWJ) A device that creates repeated droplet impingement on the surface by splitting continuous water jet into discrete clusters. The formation of liquid clusters is achieved by the piezoelectric sonotrode. The sonotrode creates pressure fluctuations in the chamber with pressurized water and these are transformed into velocity fluctuations when water jet leaves the nozzle. The velocity fluctuations lead to separation of the jet into the water clusters [11].

3. Aims of the work

The innovative approach in this work simulates water droplet impingement by controlling technological parameters of ultrasonically induced PWJ. This allows achievement of a high number of impingements in relatively short time.

This work aims to define more precisely the erosion incubation stage and elucidate the mechanisms leading to initial material removal. This research area is currently highly unexplored, especially in material sub-surface layers. The work is profoundly focused on electron microscopy techniques supplemented by microhardness measurement to describe the surface and subsurface changes. The highlight of this work is the proposal of an inventive EBSD measurement methodology that allows to directly observe selected material grains before and after exposure to liquid cluster impingements. Compared to standard evaluation based on roughness this technique gathers information about induced misorientation inside the grains and provides information from a thin subsurface layer.

The first part of this work is focused on processes happening inside the material preceding macro-material removal and the second part is focused on using these processes in controlled manner. The main output of this study will be beneficial for understanding the early erosion processes based on exposure time or impact distribution. The next important area of this work is to describe the transition between erosion stage I and II. Finally, the technical use of this knowledge will be demonstrated as a mean of surface hardening and roughening. Knowledge of the effect of increasing number of water clusters impingement on the surface of structural materials may in greater scope be used for more precise prediction of initial erosion rates.

The effect of impingement distribution and standoff distance on the surface profile of 316L stainless steel will be evaluated. The knowledge learned will be used for further study of the incubation stage and incubation stage transition to stage II on austenitic stainless steel 316L with the following goals.

- The goal is to describe processes on the surface and subsurface of the material induced by water cluster impingement in the erosion incubation stage.
- The processes leading to the transition between the incubation erosion stage and erosion stage II leading to macroscopic material removal will be described.
- The hardness profile caused by repeated water cluster impingement will be evaluated in the case of selected material.
- The surface roughening during the erosion incubation stage will be described based on liquid cluster parameters in the erosion incubation stage and transition to erosion stage II.
- The methodology for erosion incubation stage evaluation will be developed and tested.

4. Experiment

4.1. Austenitic stainless steel 316L

The AISI 316L steel was selected as experimental material. The 316L stainless steel was chosen due to its high plasticity and its structural homogeneity, making it favourable for incubation erosion stage testing.

Austenitic stainless steel 316L was supplied in the form of a hot-rolled plate. The material shows structural homogeneity. Therefore, it allows for precise and repeatable incubation erosion stage measurements such as microhardness measurement. The chosen properties of experimental material are shown in **Table 1** The grain size was evaluated using EBSD. Hardness was measured using Duramin microhardness tester (Struers, Denmark) with a load of 1.96 *N* and tensile properties were evaluated using MTS 810 servo-hydraulic testing machine (MTS, USA).

Table 1 Selected properties of experimental material 316L steel

Material	Elasticity modulus *GPa*	Tensile yield strength *MPa*	Tensile ultimate strength *MPa*	Arithmetic mean grain size μm	Area weighted mean grain size μm	Hardness HV0.2
316L steel	198	322	625	*10.38 ± 7.14 16.33 ± 12.34	*19.86 ± 12.88 32.42 ± 20.57	184 ± 10

* A value that considers the twin boundaries as grain boundaries

Figure 3 shows an EBSD analysis of the surface of 316L stainless steel in the as received state. Area of the scan was 700x200 μm with step size of 0.5 µm. **Figure 3** shows grain orientation map with grain boundaries and inverse pole figure in the inset. The pole figure analysis shows preferred crystallographic plane orientations; however, the MUD reaches only value of 1.26, indicating very low crystallographic texture.

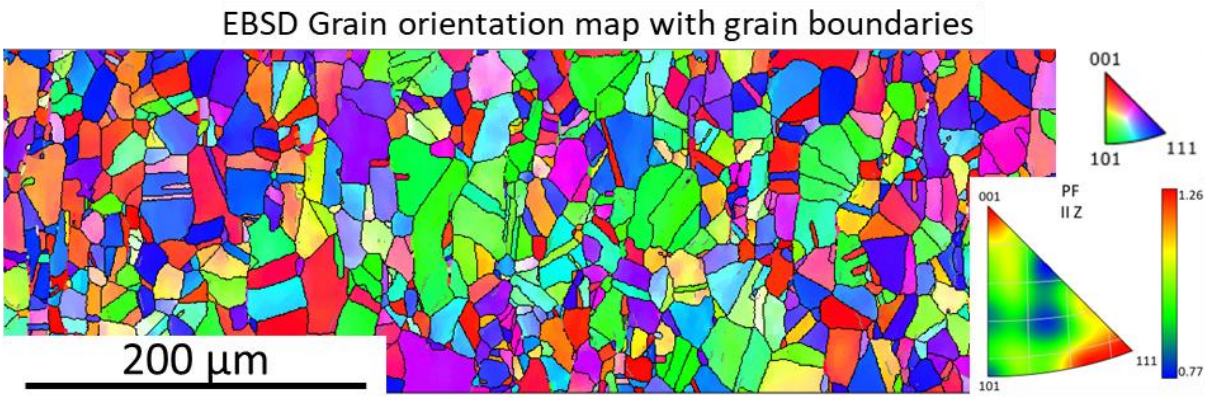

Figure 3 EBSD analysis of as received AISI316L surface to be treated by PWJ showing EBSD grain orientation map with grain boundaries (black) and IPF parallel to Z in the inset.

4.2. Overview of experiments

The technology used for water exposure of surfaces in this experiment is the PWJ system located at the Institute of Geonics UGN CAS. The important part of the system is the sonotrode

oscillating based on an acoustic generator ECOSON WJ-UG 630-40 (Ecoson, Slovakia). The sonotrode with the frequency of 40 *kHz* was chosen for the experiments. The experiments are divided into sets based on development period and experimental goal.

The first set of experiments (Table 2) deal with PWJ traveling on a line on austenitic stainless steel 316L

The 316L stainless steel was treated by four hydraulic pressure levels 30, 40, 50 and, 60 *MPa*. The standoff distance was varied in the first part of the experiment. The stair trajectory described by Hloch et al. [16] was used to estimate the optimal standoff distance in this experiment. After the optimal standoff distance was estimated for each pressure level, variations in water impact distribution were examined by variations in feed rate (1,5,10 *mm/s*). The feed rate can be described as the travel speed of the working PWJ head over the material surface in a direction parallel to the surface.

Table 2 Experimental parameters of the first set of experiments

Goal of experiment	p	f	Nozzle diameter	Flow speed	Flow rate	PWJ path	Optimal standoff	Feed rate	Impingement exposure	Material
	MPa	*kHz*	*mm*	*m/s*	*l/min*	-	*mm*	*mm/s*	*i/mm*	-
parametric optimalization	30	40.7	0.5	220.7	2.6	line	28	1-5	40 000-8 000	AISI316L
	40	40.5		254.8	3.0		30			
	50	40.4	0.5	284.9	3.4	line	36	1-10	40 000-4 000	AISI316L
	60	40.7		312.1	3.7		60			

The second set of experiments (**Table 3**) focused on the investigation of the early erosion stage in the 316L stainless steel. The area of interest was erosion stage I (known as incubation) and the description of the transition between erosion stages I and II. Experiments were carried out with 40 *kHz* sonotrode and 50 *MPa* pressure in an acoustic chamber. The experiments of this set are controlled by a number of impingements on the surface of the treated area. This is achieved by variations in exposure time or feed rate. Experiments are described in **Table 3**.

Table 3 Experimental parameters of the second set of experiments

Goal of experiment	p	f	Nozzle diameter	Flow speed	Flow rate	PWJ path	Optimal standoff	Feed rate	Exposure	Material
	MPa	*kHz*	*mm*	*m/s*	*l/min*		*mm*	*mm/s*	*s*	-
surface hardening	50	40.7	0.4	284.9	2.15	spiral	60	0.33-0.05	X	316L steel
surface hardening	50	40.7	0.4	284.9	2.15	stationary	60	X	1-20s	316L steel
erosion observation	50	40.2	0.4	284.9	2.15	stationary	45	X	1-3s	316L steel

4.3. Sample preparation

Austenitic stainless-steel samples were prepared similarly. Mechanical grinding by abrasive paper of average grain sizes of 46 *μm*, 22 *μm*, 18 *μm*, and 15 *μm* was followed with polishing using diamond paste with grain size of 3 *μm* only. Both grinding and polishing were done on ATM Saphir 320 and Saphir 330 (ATM Qness, Germany). Electrolytic polishing was the final step for the preparation of EBSD compatible surfaces. Electrolytical polishing was done by the LectroPol-5 (Struers, Denmark). Treated cross-sectional samples containing erosion kerfs were cut using precise electrical discharge machining. The cross-sectional samples were then mounted using hot mounting (180 °C) carbon filled resin Polyfast (Struers, Denmark). The cross-section was then grounded and polished in a similar manner as the top surface, but instead

of electropolishing further mechanical polishing using diamond paste 1 μm and 0.25 μm was performed. Chemical mechanical polishing by OPS was the final preparation step.

4.4. Surface and subsurface observations

The quantification of the parameters of the treated surface (roughness profile, depth, removed volume) was evaluated using either non-contact profilometer MicroprofFRT (FormFactor, USA) or in case of a more precise evaluation of incubation stage by confocal microscope Olympus LEXT OLS 3100 (Olympus, Japan). The evaluation consisted of the measurement of kerf depths in erosion stage III and surface roughness of traces in erosion stages I and II. The cut off frequency of $\lambda_c = 0.8$ *mm* was chosen during roughness evaluation. The minimum length of the evaluated line was 2.5 *mm.* The parameters Rz (heigh of profile) and Rv (valley depth) were evaluated when the surface roughening was achieved.

Detailed surface observation was conducted using a scanning electron microscope (SEM) Tescan Lyra 3 XMH FEG/SEMxFIB (Tescan, Czech Republic). The microscope is equipped with the EBSD detector Symmetry, and XMax80 energy dispersive X-ray spectroscopy (EDS) both controlled by AZtec software (Oxford Instruments, United Kingdom.

For subsurface observation of dislocation distribution, lamellae were prepared from the selected surface location by focused ion beam (FIB). The lamellae were then observed using a TEM microscope JEOL JEM-2100F (Jeol, Tokyo, Japan). The EBSD was used for surface measurement of phase composition, grain size, morphology and misorientations. Grain morphology analysis was done by EBSD grain orientation map. Texture changes in PWJ treated surface were quantified by inverse pole figures (IPF), where the level of preferred orientation is expressed as multiples of uniform density (MUD). Most importantly, surface, and subsurface deformation was evaluated based on Kernell average misorientation (KAM) maps. The KAM mapping show misorientation angle of the pixel and the selected degree of its neighbouring pixels.1-degree neighbours were considered in this work. EBSD analysis can be according to some sources [17, 18] correlated to density of geometrically necessary dislocations.

The initial hardness of untreated material was measured by the Vickers hardness testing method. The load of 0.2 kg was used for evaluation of original material hardness. Tests were done by the Duramin microhardness tester (Struers, Denmark)

The effect of PWJ on material microhardness was measured on cross-sectional cuts. The microhardness tests were performed using instrumented Vickers type indenter on the Zwick Nanoindenter ZHN (Zwick Roell, Germany). The loading force was chosen to create indents with approx. 10 μm length of indent diagonal. The indent size was selected to measure close to the surface (30 μm) with minimal influence due to the sample edge. Microhardness 2D maps were created in Python 3.11.3 and interpolated by Scipy.interpolate method using linear interpolation. **Figure 4** show microhardness measurement strategy.

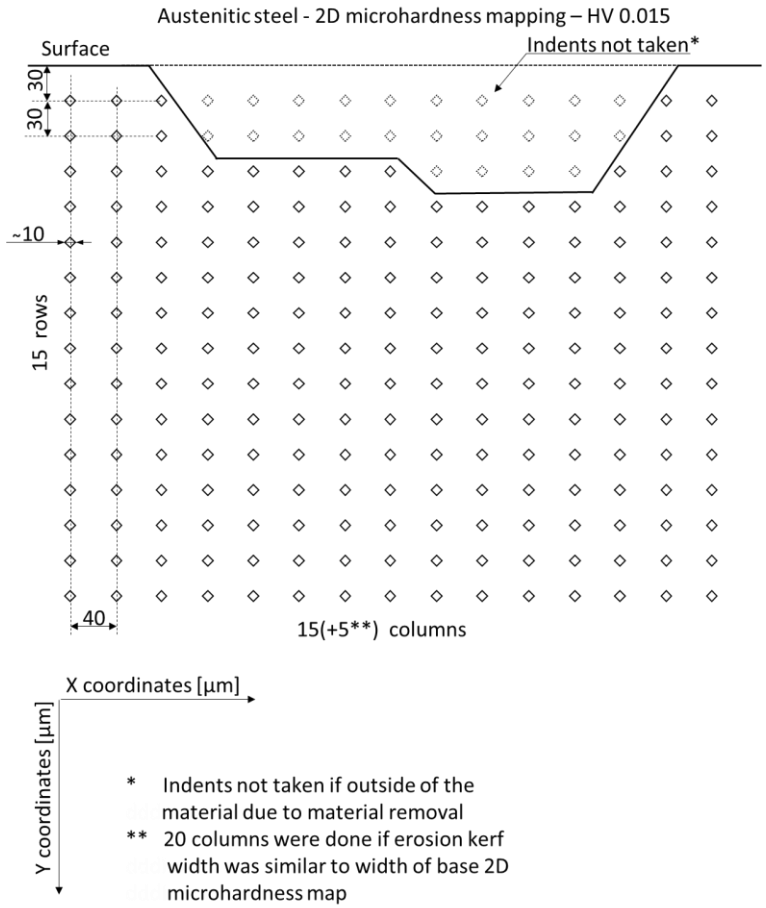

Figure 4 Schematic of microhardness measurement of PWJ treated surfaces

4.5. Fatigue testing methodology

The fatigue tests were performed using MTS 810 (MTS, USA) servo hydraulic testing machine on cylindrical samples with a gauge length of 15 *mm* and gauge diameter of 6 *mm.* Fatigue samples were prepared using turning and grinding. The samples were not subjected to any sort of heat treatment after turning. The sample's axis was in the rolling direction. The fatigue samples were polished using SiC paper with grit from 120 to 4000. The last grinding step was in a direction parallel to the sample axis. The samples were then polished using diamond pastes (3 μm, 1 μm, 0.25 μm). The samples were then treated by the PWJ. The tests were done in symmetrical (R = -1) total strain controlled mode with constant strain rate of $5x10^{-3}$ s^{-1} at an ambient temperature. Strain amplitudes selected were ε_a = 0.44; 0.32 and 0.28 %. Thermocouples touching the specimens during loading were used for checking sample temperature. The strain was measured by the MTS contact axial extensometer.

5. SELECTED Results and discussion

5.1. Experiment set I

5.1.1 Effect of water cluster distribution and development on the 316L steel

The evolution of profile parameters based on standoff distance at constant feed rate for four hydraulic pressure levels p=30, 40, 50, 60 *MPa* is depicted in **Figure 5a**. Based on Hloch et al. [16]. stair trajectory was applied in this thesis to determine the optimal standoff distance for the given hydraulic parameter. Hloch et al. [16] divided erosion regimes based on standoff distance into incubation, acceleration, culmination, depletion, and termination. These stages can be evaluated based on jet morphology or depth achieved. The optimal standoff distance evaluated within this work should overlap with the culmination regime described by Hloch et al. [16], however the stages in this work are determined by roughness parameters instead of depth. Because austenitic steel with hardness close to 200 HV 0.2 is tested, while a number of researchers [19, 20] use softer aluminium alloys for optimal standoff distance evaluation. Second reason was that the pressure/nozzle combinations chosen led to impingements of the material at subsonic velocities at a moderate feed rate of 1 *mm/s*. Lastly, samples were in a polished state to evaluate the erosion incubation changes. However, Kirols et al. [21] concluded that improving initial surface roughness is a practical tool for delaying water droplet erosion. Variation in standoff distance led to significant changes in the achieved roughness parameter Rz. Rz, and Rv both show the existence of optimal standoff distance based on the most intensive surface roughening. Based on the roughness parameter (Rz and Rv) evaluation, optimal standoff distances were selected as depicted in **Figure 5b**. The increasing standoff distance causes an increase in Rz up to optimal standoff distance and then decreasing tendency. A similar development based on standoff distance was observed for removed volume on aluminium alloy by Foldyna et al. [22]. The surface of the steel sample was then treated at selected optimal standoff distances at each pressure level with increasing feed rate. An increase in feed rate leads to a controlled decrease in the total volume of cluster by decreasing impingements per millimetre *i/mm*. The chosen feed rate values were: 1 and 5 *mm* for 30 and 40 *MPa* (lower pressure levels) and 1, 5, 10 *mm/s* in the case of 50 and 60 *MPa* (higher pressure levels). Results are shown in the form of surface profile evaluation in **Figure 5c**.

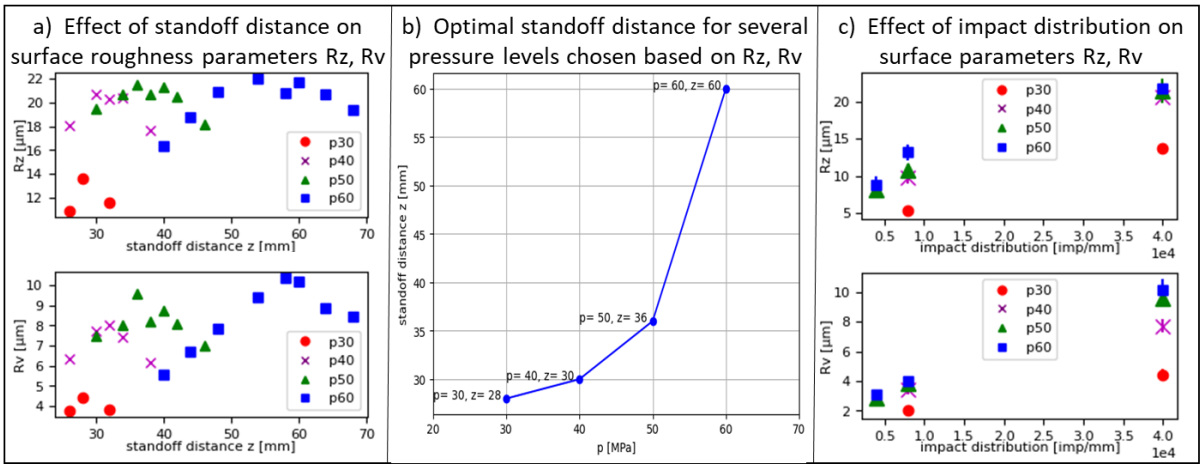

Figure 5 Roughness parameters Ra, Rz, Rp, Rv with Rsk and kurtosis Rku of 4 pressure levels based on feed rate v mm/s at optimal standoff distances z_{opt} selected for each pressure level p = 30, 40, 50, 60 MPa as 28, 30, 36, 60 mm respectively.

The pressure level variation at the feed rate of 1 *mm/s* leads to material roughening in cases of 60 *MPa*, 50 *MPa* and 30 *MPa* pressure. The PWJ treatment with 50 *MPa* pressure shows preferential places with significant damage accumulation. The creation of grain boundary exposed relief can be observed after all four hydraulic pressure levels. Rimmed grain boundaries can be observed after 60 and 50 *MPa* (1 *mm/s*) treatment. PWJ treatment with 60 *MPa* and 50 *MPa* also led to the creation of small cavities close to the elevated grain boundaries. PWJ treatment with 40 and 30 *MPa* led to exposed grain boundaries as well, but not in such magnitude. Surface steps related to twinning are apparent after treatment at the feed rate of 5 *mm/s* an in case of treatment with higher hydraulic pressures of 60 and 50 *MPa* and feed rate of 10 *mm/s*, steps are also visible.

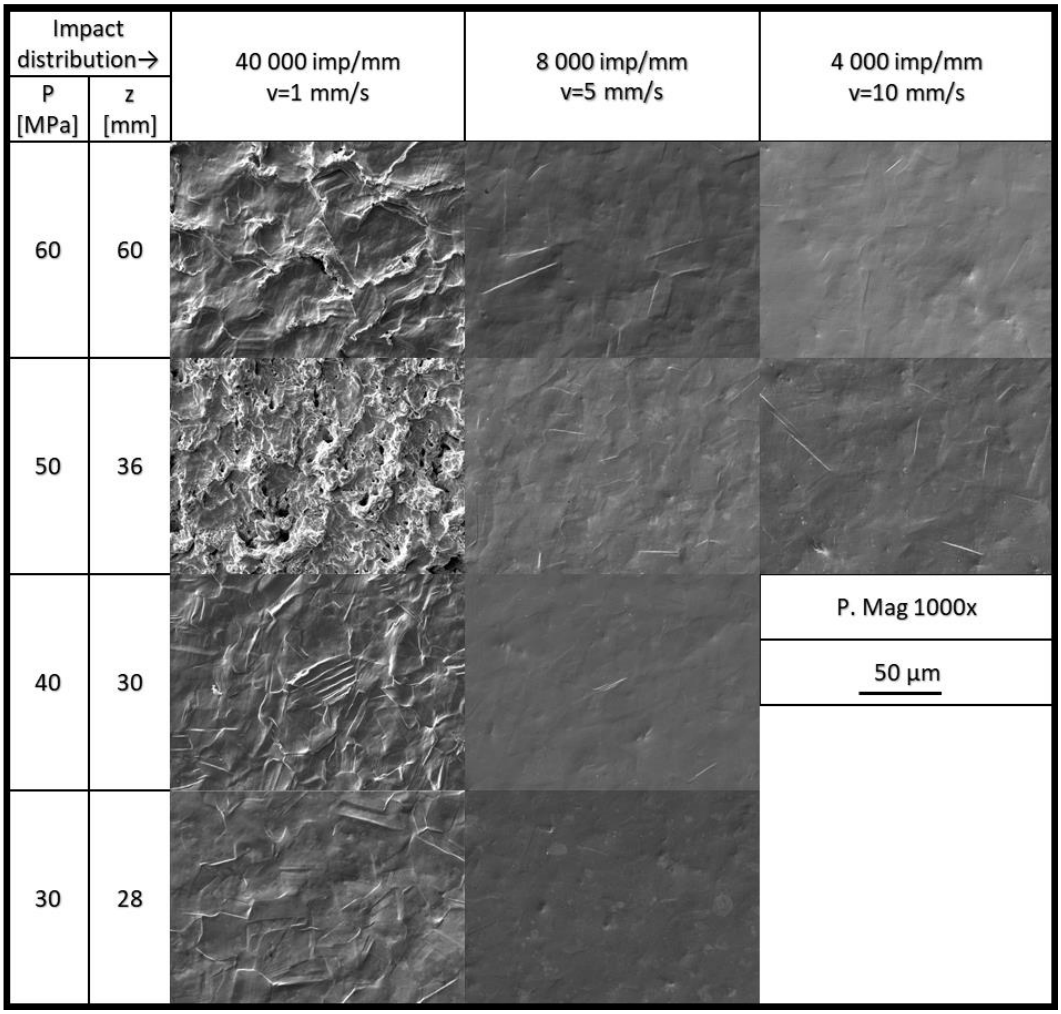

Figure 6 SEM details of eroded surface for four pressure levels at different impact distribution

5.2. Experiment set II

Experimental set II consists of PWJ treatment of stainless steel 316L. The treatment of rotatory fatigue samples was done by PWJ and compared with untreated material. The next experiment focused on changes to the surface and subsurface of the treated material caused by PWJ with varying exposure time. The last experiment focused on EBSD observation of incubation erosion stages caused by PWJ with varying exposure time.

5.2.1 Surface hardening – fatigue improvement

Fatigue samples were treated with PWJ with constant hydraulic pressure and variations in feed rate from v = 0.05 *mm/s* up to v = 0.33 *mm/s*. Fatigue tests were conducted on 3 strain levels for each treatment. Details of the fatigue testing are described in **Chapter 4.5**.

Figure 7 shows the dependence of a number of cycles to fracture N_f on total strain amplitude $\varepsilon_{at.}$ The fatigue curve of as received material was measured in large interval of total strain amplitudes. Based on the fatigue curve of as received material three strain levels 0.44, 0.32 and 0.28% were selected. Since the x-axis is plotted in logarithmic scale, the improvement of fatigue life due to the PWJ treatment is quite high. At the strain level of ε_{at} = 0.28%, two PWJ treatments with feed rates of 0.2 and 0.05 *mm/s* achieved a maximum number of cycles $7x10^5$. At this value of the applied number of cycles, the fatigue testing was interrupted/finished without the final fracture of the sample and the test was considered run-out. At the same strain level, the sample treated by PWJ at v = 0.33 *mm/s* reached a fatigue life of 106 589 cycles, which is a significant increase compared to 37 635 cycles of untreated material. The decrement in PWJ feed rate led to a number of cycles to failure increase at ε_{at} = 0.32%. The number of cycles to failure at this strain levels was in the range of 10^4 to 10^5 . A similar trend was observed at ε_{at} = 0.28%, and is even more conclusive. The number of cycles to failure ranged from 3.10^4 for an untreated sample. Specimens treated by PWJ feed rates of 0.2 and 0.05 mm/s did not fracture and the tests were stopped after 7.10^5 cycles. Possible increase of the fatigue life after PWJ treatment was suggested in a preliminary study of the UGN group by Hlaváček et al.[23] who observed improvement from N_f = 166 190 to N_f = 439 590 at stress amplitude about 290 MPa. The main difference is that they used lower pressure and sonotrode oscillating at a lower frequency of 20 kHz. S-N curve presented in their case shows that the beneficial effect of PWJ treatment on fatigue life is more dominant in low amplitude high cycle area. This observation [23] was one of the motivation for the opening of this topics as the theme for this Ph.D. thesis. The obtained results confirm for the first time, according to our knowledge, the possibility to use the PWJ as an alternative method for prolonging fatigue life, similarly, to e.g. shot peening [24]. It can be assumed that the fatigue life of samples was increased due to the introduction of the residual stresses into the surface layer of the material. Polák [25] described that compressive residual stresses may slow down fatigue crack initiation and propagation in its early stages. This may explain the positive effect of PWJ treatment at lower strain amplitudes and the lack of this effect at higher strain amplitudes. Most fatigue life is determined in the crack initiation stage at lower strain amplitude levels, while at higher strain amplitudes, fatigue life is mostly determined by the crack propagation stage.

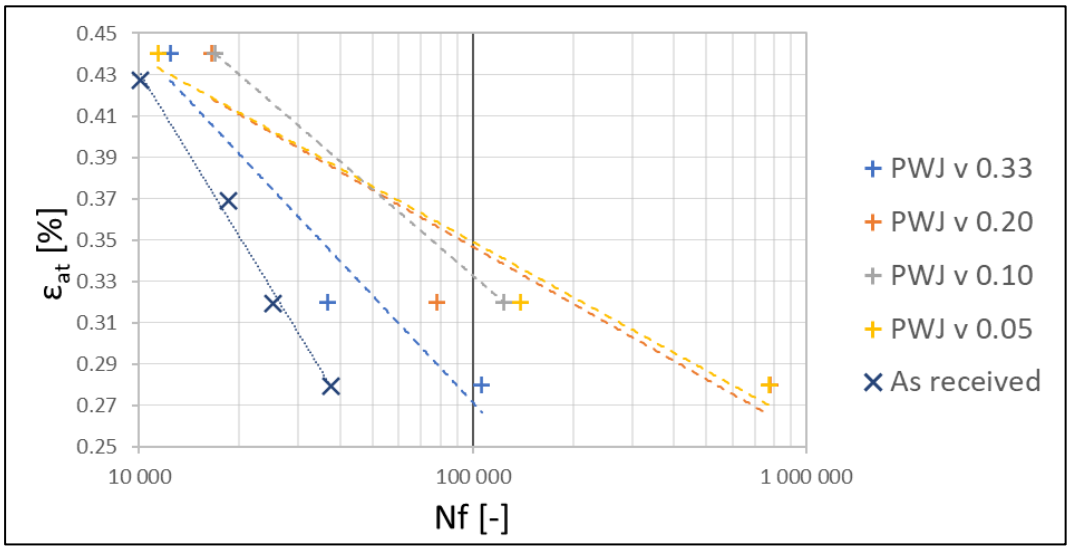

Figure 7 a) Fatigue life curves of FT 1 with variable PWJ feed rate with constant PWJ feed rate compared to fatigue life curve of untreated material. b) Detail of 10^4-10^6 area. Measurements are approximated by logarithmic trendline.

5.2.2 Surface hardening – effect of time exposure

The hydraulic pressure of 50 *MPa* was selected for the time exposure test of 316L steel. The only variable of the experiment is a number of impingements of water clusters, which is controlled by variations in exposure time f ≈ 41 *kHz*. The surface morphology after given number of water impingements was observed using SEM and followed by subsurface observation using TEM. TEM observation was carried out for a better understanding of erosion induced changes in the subsurface. Microhardness was measured under a load of 150 *mN*. Surface shape was evaluated using the MicroProfFRT non-contact profilometer.

Figure 8 shows the surface of steel samples observed using SEM and treated by PWJ for exposure times of 5, 10 and 20 seconds, which is approximately 205 000, 410 000 and 820 000 impacts respectively. The experiment contains all 3 erosion stages.

Figure 8a shows the area subjected to PWJ for 5s. It corresponds to approximately 205 000 impingements. The centre of the eroded area shows a high level of deformation. Outside of the centre region the surface appears gradually less damaged. The detail of the centre area is shown in **Figure 8b**. The detail shows number of protruding regions. Occasional presence of microcavities was observed.

After 10 *s* of PWJ exposure (**Figure 8c**) which equates to about 410 000 impingements the roughened area is wider than the diameter of the used nozzle. The area gets gradually more deformed closer to the jet core. The area under the jet core shows a significant number of cracks and microcavities, as well as places of visible material removal. Detail in **Figure 8d** shows the centre of exposed area, where the material removal process is most apparent.

PWJ exposure of 20 *s* of PWJ (**Figure 8e**) led to significant material removal in an area under the jet core. The top and side edges of the erosion kerf are surrounded by the pile-up. However, the bottom part of the kerf shows a gradual transition into a roughened area with no significant pile-up. The detail (**Figure 8f**) focuses on pile-up on the top side of the erosion kerf. There are visible surface steps behind the pile-up. The pile-up is also disturbed by surface cavities and visible tearing of the pile-up was observed. Three quarters of the kerf edge had pile-up and one quarter of the kerf edge showed a continuous transition to unaffected material similarly as

observed in [19]. The eroded area shows asymmetric erosion distribution., that can be attributed to several possible factors. Firstly, the water inlet is asymmetrically connected to acoustic chamber, which could create asymmetry in acoustic waves propagation and therefore in the water clusters. The second possible cause is that even a slight deviation of perpendicularity between the jet and the treated surface may cause an asymmetric commence time of the lateral outflow similar to case of radial surfaces as described by Burson-Thomas et al. [26]. Also, imperfections in the geometry of the output nozzle can influence the shape of the jet.

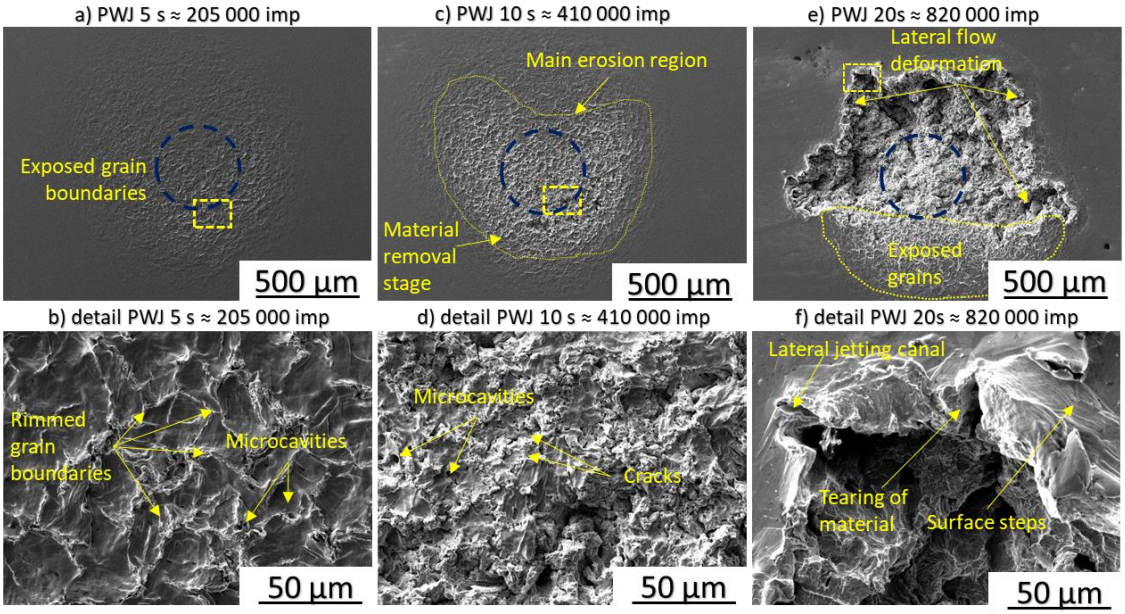

Figure 8 SEM analysis of surface treated with increasing time under water impingements at frequency of impingements of 41 kHz for erosion time of a)5 s b) 10 s. Blue circle mark jet diameter

Figure 9 shows depth plot of the dependences of removal volume and erosion depth achieved by increasing the exposure time of PWJ from 1s up to 20 s. Sufficient surface depression for detection using a profilometer is created roughly after 3 s (123 000 *imp.*) of PWJ. The material erosion evaluated through depth and volume removed, grows gradually with an increase in exposure time (number of impingement) in the measured region. The erosion depth h increment was fitted with the curve defined by Eq. (3), where the only input is the exposure time (i.e., number of impingements):

$$h_e = 0.0112t^{3.3308} \tag{3}$$

Removed volume can be then expressed by the Eq. (4):

$$v_r = 0.0034e^{0.1822t} \tag{4}$$

where d_t is the depth in the μm, v_r is volume removed in mm^3 and t is time in s. The selected equation types were selected to maximize the fit and the R^2 values, shown in **Figure 9**.

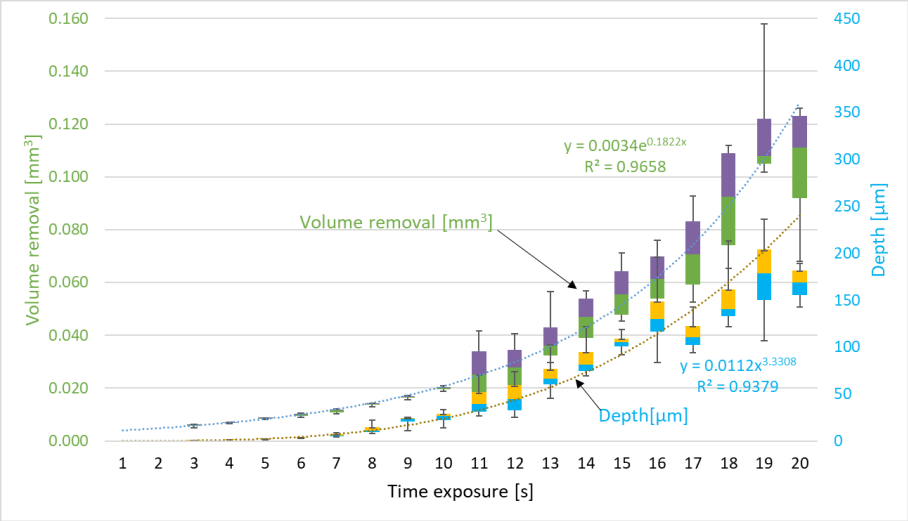

Figure 9 Box graph of depth and volume removal based on PWJ exposure ranging from 1s to 20 s.

The results of microhardness are presented in microhardness/depth dependence graph. each row of microhardness values under the surface was averaged and plotted (**Figure 10**) The depth-hardness curves show an increase in area bellow 100 μm. From the original surface micro-hardness of 294 HV 0.015, the hardness increased to 316 HV 0.015 after 10 *s* of PWJ exposure. For other exposure times of 5 *s* 15 *s* and 20 *s* the surface hardness is similar from a statistical point of view to the untreated surface.

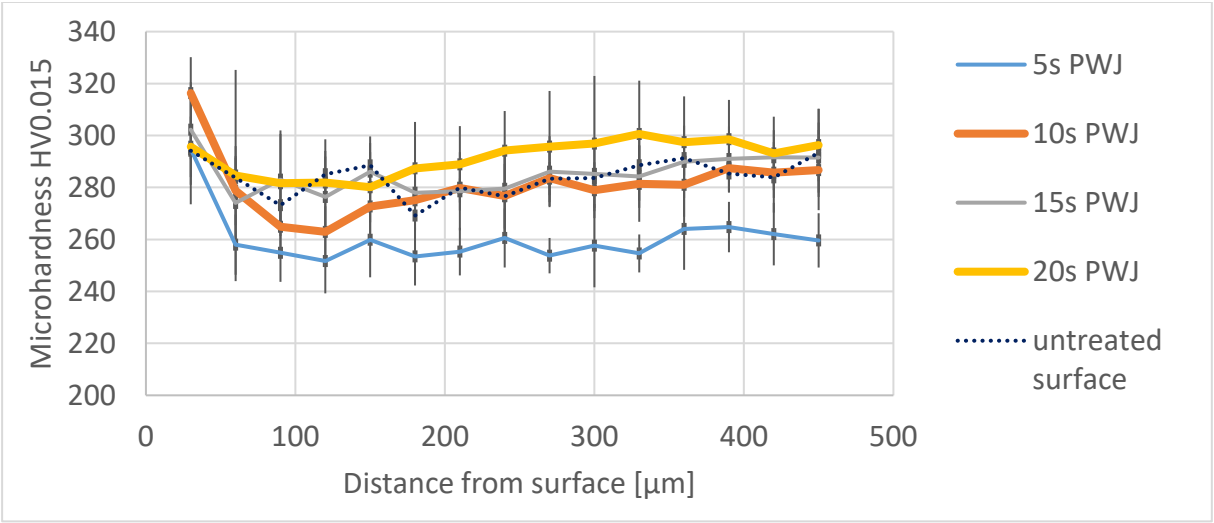

Figure 10 Hardness-depth profile of surface treated with different PWJ exposure times ranging from 5 s up to 20 s

The subsurface hardening is shown in 2D visualization in **Figure 11**. Before the plot each value was normalized, this was done by dividing each value by the map average. The values plotted therefore show hardening related to 2D measured area. The visualization was done by a software written in Python with linear interpolation between the points. The visualization shows the formation of the hardened layer under the first row of indents after 5 *s* of PWJ exposure. The first row is located 30 μm under the treated surface. It can be assumed based on the measured hardness gradient, that hardening increases closer to the surface.

The first layer of indents shows stronger hardening after 10 *s* of PWJ exposure. Moreover, the hardened layer is more homogenously spread across all the indents in the first row and some

indents of second row also show hardening. After 15 *s* of PWJ exposure, a significant erosion kerf was created in the cross-section. From the first layer of indents under the kerf the hardening can be observed, however homogenous hardened layer is missing. The most significant hardening is visible close to kerf edges and radiuses in the first measured row under the kerf. The treatment using 20 *s* of PWJ exposure results in similar situation as for 15 *s* exposure

Hardening to depth below 100 µm has been observed in this work in this work on austenitic steel 316L and a similar hardness depth was achieved by Chlupová et al. [27] on EA4T ferritic steel. The depth of hardened layer observed in this work is quite shallow compared to shot peening or laser peening. The hardening profile cause by PWJ will now be compared to other methods of surface hardening. Shot peening of AISI 316L led to an increase from 220HV to 405HV with a hardened layer depth of about 300 µm, as measured by Ahmed et al. [28]. A similar depth (~300 µm) was achieved by Maleki et al. on AISI 1060 using the Taguchi approach. LSP achieved over 600 µm for AISI 316L as measured by Wang et al. [29] In the case of Ti alloys treated by LSP, a depth over 400 µm was achieved for Ti17 [30] and a similar depth in the case of Ti6Al4V [31]. Other authors studying ultrasonic PWJ either observed no change or statistically negligible change as is the case of Stolarik et al. [32] on EN-AW1050A or Nag et al. [33] on AW6060 .The hardening to a depth around 200 µm or deeper has been observed by Lehocka et al. [34], Hloch et al. [35] and Srivastava et al. [8, 36, 37]on 304 austenitic stainless steel. Interestingly, Lehocka et al. [34] compared AISI304 hardening depth which reached 250µm to aluminium alloy EN AW 6060 where no significant hardening was observed.

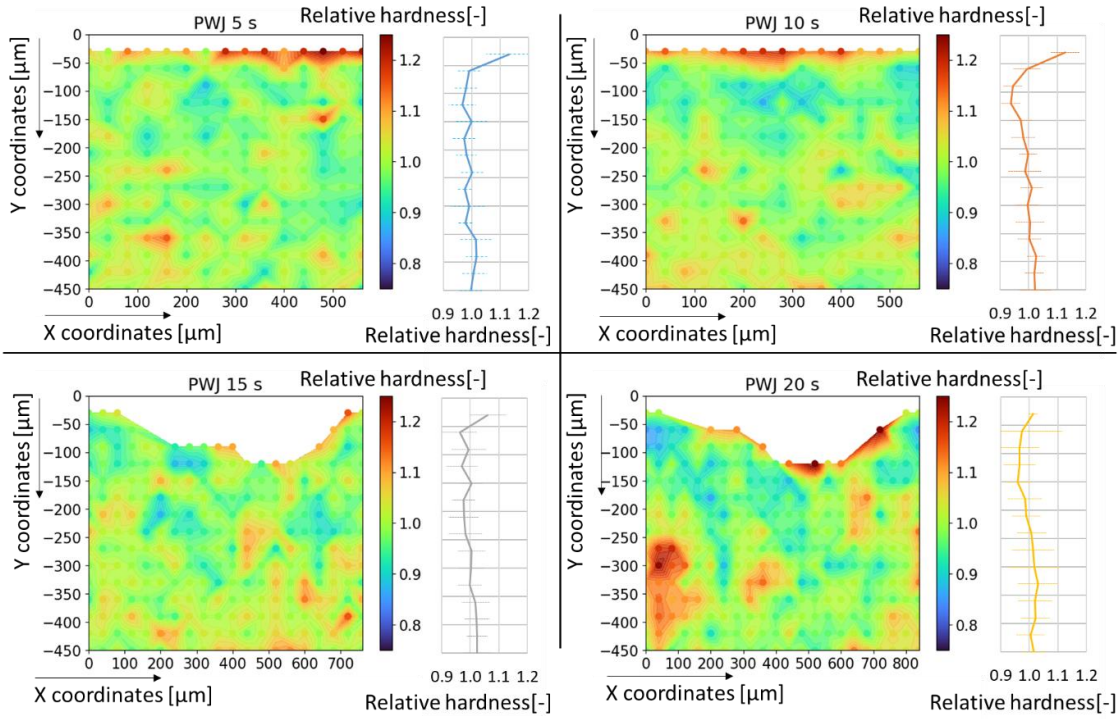

Figure 11 Relative 2D hardness maps with the addition of averaged values across each depth layer

Figure 12a shows relatively high dislocation density approximately 10^{13} m^{-2} of material state before PWJ exposure contains due to manufacturing history (hot rolling). Dislocations gliding on multiple slip systems are relatively homogeneously distributed. Dislocation pile-ups can be observed close to grain boundaries. Furthermore, dislocations forming close packed nets were

observed close to grain boundaries. An example of dislocation structure after exposure to PWJ for 5 *s* is in **Figure 12b**. The grain in the picture is approximately 2 μm under the treated surface. It shows high density of dislocations estimated as 7.10^{14} m^{-2}. The dislocations are homogenously distributed without signs of arrangement into wall or cell structures often observed in cyclically loaded samples. Before PWJ treatment mostly dislocations from one slip system are visible, while after PWJ exposure multiple slip systems appear active.

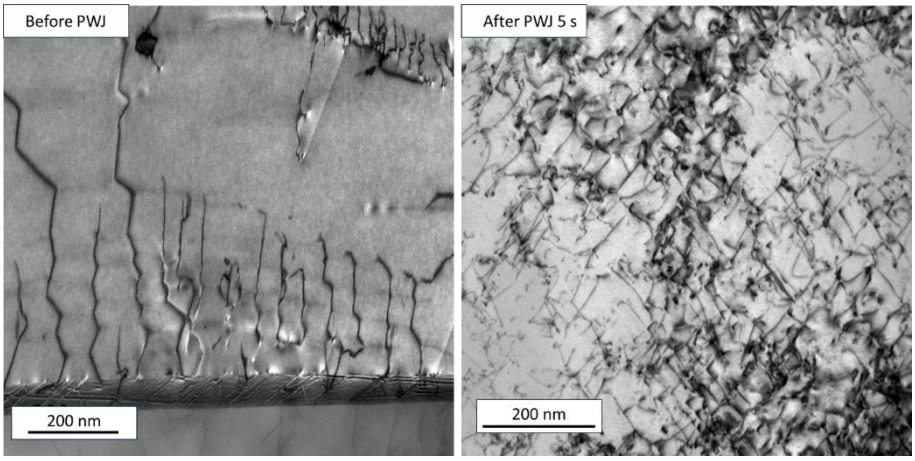

Figure 12 Comparison of dislocation structure observed by TEM in subsurface prior to PWJ treatment and after 5s of PWJ exposure

The results suggest that the hardness increases significantly closer to the surface than 30 μm. and measured hardness gradient confirm this finding. Based on these findings last experiment was designed to measure kernel averaged misorientation of surface treated by PWJ to quantify large area changes in the subsurface layer.

5.2.3 Erosion incubation stage EBSD observation

The experiment described in the previous chapter proved the hardening under the surface treated by PWJ, however only in a very thin layer under the surface. That is the reason why a new measurement methodology was derived to record changes in the layer closest to the surface. The surface of the samples was electrolytically polished and then marked by small hardness indents in a circle pattern according to the schematic shown in **Figure 13a**. **Figure 13b** show an OM micrograph of the marked surface. The marked areas were measured by EBSD prior to PWJ exposure. After EBSD measurement, areas were subjected to selected exposure times of PWJ and then again analyzed using EBSD. The process of scanning was performed inside the circular area in a cross pattern due to the inhomogeneity of water cluster distribution in PWJ. Note how areas B and D were not treated in order to limit possibility of influence between adjacent areas

Figure 13c shows the forward scattered electron (FSE) image of an area treated by PWJ with 3 *s* exposure which is the maximum exposure time used in this experiment. The EBSD grain orientation map overlay was inserted into the image. While the treated area is visibly circular, approximately half of the area is significantly roughened while the other half shows much lesser roughening. In the most roughened area, the EBSD overlay shows a number of black areas called non indexed regions (NIR). In these regions, it was not possible to index the orientation of grains using the Kikuchi pattern.

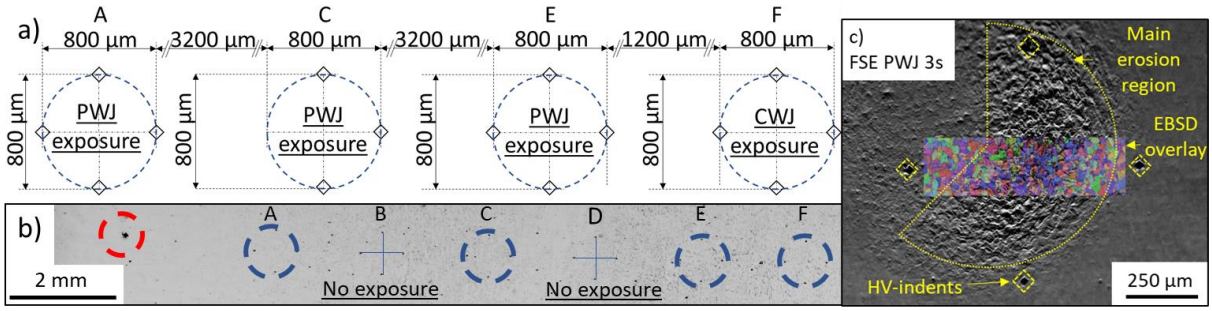

Figure 13 Schematic for EBSD measurement preparation showing a schematic of marking b) the electropolished surface prepared for EBSD with marking c) detail of marked and PWJ treated area with indicated EBSD overlay

Figure 14 shows an detail of EBSD of area before and after 1 s of PWJ exposure and a different area before and after 3 s of PWJ exposure. Detail for 1s exposure shows that non-indexed regions (NIR) are present since this very short exposure, and they are concentrated mainly to the vicinity of grain boundaries. The increase in PWJ exposure time leads to increase in number of non-indexed regions. The most possible reason in our case is increase of roughness of the exposed surface. After 3s of PWJ exposure a misorientation induced inside grains is visible even in EBSD grain orientation map by colour gradients inside larger grains. The gradient suggest that the grain tilting is mechanism that is behind the surface roughening. SEM observations in this thesis as well as observations done by other authors [10, 15, 38–40], claim that the surface irregularities in the incubation erosion stage are created by grain tilting. EBSD measure the orientation of each pixel, replicating grain morphology in the form of an EBSD grain orientation map. Changes in grains in the EBSD grain orientation map signify tiling of the top layer of the grains. It is important to note that the backscattered electrons, bringing the information about the specimen's crystallography, comes from relatively thin surface layer less than 1µm. The observed change of crystallographic orientation due to PWJ exposure is related to this thin surface layer and no information is gained about the situation deeper from the surface.

For further quantification of misorientation inside grains, an analysis using kernel averaged misorientation (KAM) was performed. KAM provides a possibility to characterize plastic deformation induced by PWJ by a number. Picture for as received state is taken from the same area as picture for 1s of PWJ exposure. The red lines are grain boundaries or twins, while the colour gradient inside the grains displays misorientations inside the grains. It is necessary to notice that the KAM map shows some misorientations in the interior of the grains even in as received state, i.e., before PWJ treatment, however their presence is significantly increased after PWJ exposure, mainly in form of low angle boundaries (LAB).

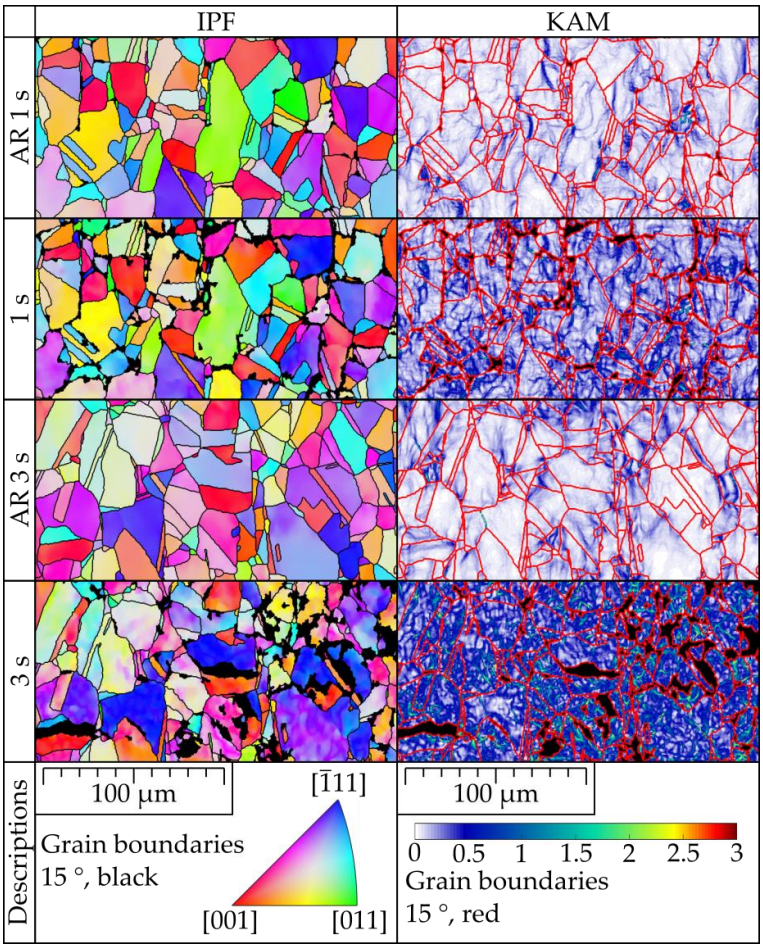

Figure 14 Comparison of area before PWJ treatment and after 1 s, 3 s of PWJ exposure. The area is observed by means of EBSD grain orientation map (right) and KAM (left).

Since the origin of NIR regions is of crucial importance, most prominent NIR regions on surface exposed to 3s of PWJ (**Figure 15a**) were closer examined by SE. The NIR regions selected for observation are marked in **Figure 15b**. **Figure 15c** show significant surface step surrounding grain. The **Figure 15d** shows severely deformed surface step across the grain. Both of the examined NIR regions suggest that NIR regions are not created by material removal. Rather these regions appear adjacent to surface steps which deviate the angle between the surface and the electron beam.

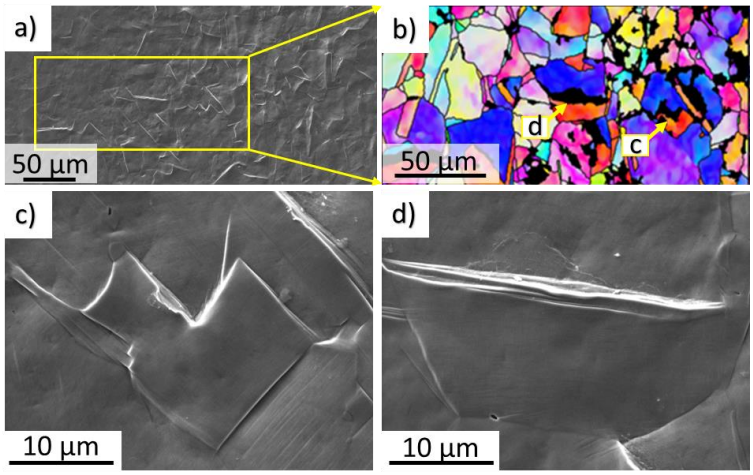

Figure 15 Detailed observation of NIR regions after 3s PWJ treatment using SE

The KAM angle was averaged across the entire examined area. Graph in **Figure 16** shows the increase in average KAM from 0.12° for as received state up to 0.21° after 1s of PWJ exposure, then further increase to 0.28° after 1.5 *s* of PWJ exposure. These values are comparable to 3 *s* of CWJ exposure 0.18° and 6 *s* of CWJ exposure 0.25°. This shows the clear advantage of PWJ over CWJ as a very effective method of material surface modification.

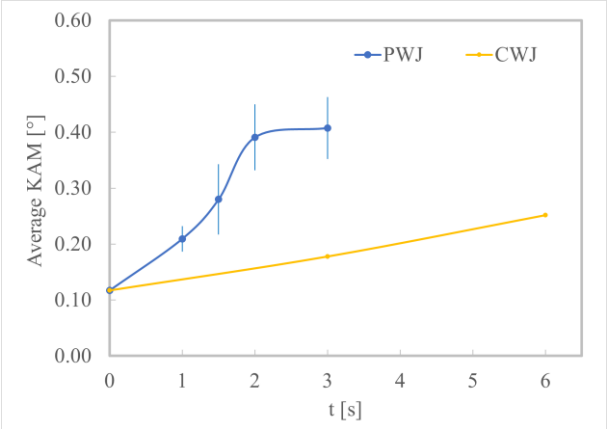

Figure 16 Dependence of averaged KAM of PWJ and CWJ on the exposure time

The KAM can be averaged across the whole eroded area. **This gives researchers tool for effectively quantifying the incubation erosion stage.** In the next paragraph, the advantages and disadvantages of this method compared to other methods for incubation stage observations will be discussed. The method shows several specific requirements considering surface preparation and is also limited by the upper erosion limit as seen by increase of NIR.

A number of authors [41, 42] propose that KAM evaluation of EBSD measurement can be used to estimate dislocation density. Liang et al. [41] compared methods for dislocation detection based on literature survey and concluded that XRD probe size typically ranges from hundreds of microns to several millimetres and the lower probe size of EBSD is about 100nm, while TEM allows the visualization of dislocation lines and dislocation density quantification at nanoscale. The main advantage of the EBSD method over TEM is the area examined. TEM lamellae prepared by FIB are of dimensions of 10-15 μm width, 8-10 μm high and 50-100 nm thick according to [43]. So, while TEM provides high accuracy of results up to analysis of single dislocations, it is local in nature which leads to poor statistical relevance [17]. The EBSD measured area in this work is 700x200 μm dimensions, which is not even the upper limit of the EBSD method.

6. Conclusions

Effect of water impact distribution and development on the surface of 316L steel was evaluated. Controlling factor of water cluster development was standoff distance. Variance in feed rate of linear PWJ path was used to control impact distribution.

- Rz value in dependence on standoff distance shows increasing tendency up to culmination and then a decrease.
- Based on surface profile measurement the optimal standoff distances were determined.
- The increase in feed rate shows strictly decreasing tendencies in Rz and Rv parameters.

Surface hardening – fatigue experiments were conducted using the pressure level of 50 *MPa* on austenitic stainless steel 316L. First PWJ was used to treat the round fatigue samples at varying cluster distribution.

- Specimens after PWJ treatment achieved significantly longer fatigue life in medium and low total strain amplitudes compared to untreated specimens.
- The increase in fatigue life showed clear dependence on the water impact distribution at ε_{at} = 0.32 %.
- Specimens treated by PWJ feed rates of 0.2 and 0.05 mm/s did not fracture at ε_{at} = 0.28 %. and the tests were stopped after 7.10^5 cycles.
- Increase of the fatigue life of specimens treated by PWJ with carefully chosen parameters is documented. This result show that PWJ is an alternative to known methods of surface hardening like shot peening.

Surface hardening – effect of time exposure experiment was conducted using static PWJ head with increasing time exposure.

- The main observed erosion mechanism in incubation stage was subsurface layer grain tilting accommodated by twining leading to exposing grain boundaries.
- The first erosion damage has been observed at the exposed grain boundaries.
- The most intense primary hardening was observed in subsurface area (30 μm).
- The hardening reached the highest values prior to start of material removal.

Erosion incubation stage EBSD observation was proposed. A methodology for quantification of the incubation erosion stage was proposed. The method uses EBSD observation of the exact surface before and after liquid clusters impingement.

- The EBSD quantification method provided both qualitative and quantitative results in early incubation erosion stages and is already considered for further experiments.
- The KAM parameter calculated based on EBSD maps can be correlated with PWJ and CWJ exposure time for quantitative analysis of incubation erosion stage.
- EBSD grain orientation map proves that grain deformation is the mechanism behind surface roughening observed in this work during the incubation erosion stage.
- The KAM evaluation shows misorientation localization into low angle boundaries.

7. References

1. BARTOLOMÉ, Luis and TEUWEN, Julie. Prospective challenges in the experimentation of the rain erosion on the leading edge of wind turbine blades. *Wind Energy*. January 2019. Vol. 22, no. 1, p. 140–151. DOI 10.1002/we.2272.

2. ELHADI IBRAHIM, Mohamed and MEDRAJ, Mamoun. Water Droplet Erosion of Wind Turbine Blades: Mechanics, Testing, Modeling and Future Perspectives. *Materials*. 31 December 2019. Vol. 13, no. 1, p. 157. DOI 10.3390/ma13010157.

3. AHMAD, M., CASEY, M. and SÜRKEN, N. Experimental assessment of droplet impact erosion resistance of steam turbine blade materials. *Wear*. September 2009. Vol. 267, no. 9–10, p. 1605–1618. DOI 10.1016/j.wear.2009.06.012.

4. GOHARDANI, Omid. Impact of erosion testing aspects on current and future flight conditions. *Progress in Aerospace Sciences*. May 2011. Vol. 47, no. 4, p. 280–303. DOI 10.1016/j.paerosci.2011.04.001.

5. ZHANG, Huang, MA, Yue, HU, Guang and LIU, Qianfeng. Droplet impaction in nuclear installations and safety analysis: Phenomena, findings and approaches. *Nuclear Engineering and Design*. September 2020. Vol. 366, p. 110757. DOI 10.1016/j.nucengdes.2020.110757.

6. LEE, Y.S., LEE, S.H. and HWANG, K.M. Cause Analysis of Flow Accelerated Corrosion and Erosion-Corrosion Cases in Korea Nuclear Power Plants. *Corrosion Science and Technology*. 31 August 2016. Vol. 15, no. 4, p. 182–188. DOI 10.14773/CST.2016.15.4.182.

7. CHOI, Duk Hyun, KIM, Kyung Hoon and KIM, Hyung Joon. Long-term investigation of erosion behaviors on metal surfaces by impingement of liquid droplet with high-speed. *Journal of Mechanical Science and Technology*. March 2015. Vol. 29, no. 3, p. 1085–1091. DOI 10.1007/s12206-015-0220-0.

8. SRIVASTAVA, Madhulika, HLOCH, Sergej, KREJCI, Lucie, CHATTOPADHYAYA, Somnath, DIXIT, Amit Rai and FOLDYNA, Josef. Residual stress and surface properties of stainless steel welded joints induced by ultrasonic pulsed water jet peening. *Measurement*. October 2018. Vol. 127, p. 453–462. DOI 10.1016/j.measurement.2018.06.012.

9. COOK S.S. Erosion by water-hammer. *Proceedings of the Royal Society of London. Series A, Containing Papers of a Mathematical and Physical Character*. 2 July 1928. Vol. 119, no. 783, p. 481–488. DOI 10.1098/rspa.1928.0107.

10. HANCOX, N. L. and BRUNTON, J. H. The Erosion of Solids by the Repeated Impact of Liquid Drops. *Philosophical Transactions of the Royal Society of London. Series A, Mathematical and Physical Sciences*. 1966. Vol. 260, no. 1110, p. 121–139.

11. FOLDYNA, Josef, SITEK, Libor, ŠVEHLA, Branislav and ŠVEHLA, Štefan. Utilization of ultrasound to enhance high-speed water jet effects. *Ultrasonics Sonochemistry*. May 2004. Vol. 11, no. 3–4, p. 131–137. DOI 10.1016/j.ultsonch.2004.01.008.

12. BOWDEN F. P. and FIELD J. E. The brittle fracture of solids by liquid impact, by solid impact, and by shock. *Proceedings of the Royal Society of London. Series A.*

Mathematical and Physical Sciences. 24 November 1964. Vol. 282, no. 1390, p. 331–352. DOI 10.1098/rspa.1964.0236.

13. BARGMANN, Heinz W. The mechanics of erosion by liquid and solid impact. *International Journal of Solids and Structures*. 1992. Vol. 29, no. 14–15, p. 1685–1698. DOI 10.1016/0020-7683(92)90162-M.

14. BURSON-THOMAS, Charles B., WELLMAN, Richard, HARVEY, Terry J. and WOOD, Robert J.K. Water droplet erosion of aeroengine fan blades: The importance of form. *Wear*. April 2019. Vol. 426–427, p. 507–517. DOI 10.1016/j.wear.2018.12.030.

15. Drop impingement erosion of metals. *Proceedings of the Royal Society of London. A. Mathematical and Physical Sciences*. 27 January 1970. Vol. 314, no. 1519, p. 549–565. DOI 10.1098/rspa.1970.0022.

16. HLOCH, Sergej, SRIVASTAVA, Madhulika, NAG, Akash, MÜLLER, Miroslav, HROMASOVÁ, Monika, SVOBODOVÁ, Jaroslava, KRUML, Tomáš and CHLUPOVÁ, Alice. Effect of pressure of pulsating water jet moving along stair trajectory on erosion depth, surface morphology and microhardness. *Wear*. July 2020. Vol. 452–453, p. 203278. DOI 10.1016/j.wear.2020.203278.

17. MOUSSA, C., BERNACKI, M., BESNARD, R. and BOZZOLO, N. Statistical analysis of dislocations and dislocation boundaries from EBSD data. *Ultramicroscopy*. August 2017. Vol. 179, p. 63–72. DOI 10.1016/j.ultramic.2017.04.005.

18. RUGGLES, T.J., YOO, Y.S.J., DUNLAP, B.E., CRIMP, M.A. and KACHER, J. Correlating results from high resolution EBSD with TEM- and ECCI-based dislocation microscopy: Approaching single dislocation sensitivity via noise reduction. *Ultramicroscopy*. March 2020. Vol. 210, p. 112927. DOI 10.1016/j.ultramic.2019.112927.

19. HLOCH, Sergej, ADAMČÍK, Pavel, NAG, Akash, SRIVASTAVA, Madhulika, ČUHA, Dominik, MÜLLER, Miroslav, HROMASOVÁ, Monika and KLICH, Jiří. Hydrodynamic ductile erosion of aluminium by a pulsed water jet moving in an inclined trajectory. *Wear*. June 2019. Vol. 428–429, p. 178–192. DOI 10.1016/j.wear.2019.03.015.

20. NAG, Akash, HLOCH, Sergej, ČUHA, Dominik, DIXIT, Amit Rai, TOZAN, Hakan, PETRŮ, Jana, HROMASOVÁ, Monika and MÜLLER, Miroslav. Acoustic chamber length performance analysis in ultrasonic pulsating water jet erosion of ductile material. *Journal of Manufacturing Processes*. November 2019. Vol. 47, p. 347–356. DOI 10.1016/j.jmapro.2019.10.008.

21. KIROLS, H.S., KEVORKOV, D., UIHLEIN, A. and MEDRAJ, M. The effect of initial surface roughness on water droplet erosion behaviour. *Wear*. November 2015. Vol. 342–343, p. 198–209. DOI 10.1016/j.wear.2015.08.019.

22. FOLDYNA, J., SITEK, L., ŠČUČKA, J., MARTINEC, P., VALÍČEK, J. and PÁLENÍKOVÁ, K. Effects of pulsating water jet impact on aluminium surface. *Journal of Materials Processing Technology*. November 2009. Vol. 209, no. 20, p. 6174–6180. DOI 10.1016/j.jmatprotec.2009.06.004.

23. HLAVÁČEK, Petr, KRUML, Tomáš, FOLDYNA, Jozef, TOBIÁŠ, Jiří, MAN Jiří. Effect of Pulsating Water Jet Peening on 316L Stainless Steel. In: Water Jet 2015 – *Research Development, Applications.* October 2015.p.29–36. ISBN: 978-80-86407-56-2

24. MALEKI, Erfan, UNAL, Okan, GUAGLIANO, Mario and BAGHERIFARD, Sara. Analysing the Fatigue Behaviour and Residual Stress Relaxation of Gradient Nano-Structured 316L Steel Subjected to the Shot Peening via Deep Learning Approach. *Metals and Materials International*. January 2022. Vol. 28, no. 1, p. 112–131. DOI 10.1007/s12540-021-00995-8.

25. POLÁK, Jaroslav. *Cyclic plasticity and low cycle fatigue life of metals*. . Prag : Academia, 1991. ISBN 978-80-200-0008-8.

26. BURSON-THOMAS, Charles B., WELLMAN, Richard, HARVEY, Terry J. and WOOD, Robert J. K. Importance of Surface Curvature in Modeling Droplet Impingement on Fan Blades. *Journal of Engineering for Gas Turbines and Power*. 1 March 2019. Vol. 141, no. 3, p. 031005. DOI 10.1115/1.4041149.

27. CHLUPOVÁ, Alice, HLOCH, Sergej, NAG, Akash, ŠULÁK, Ivo and KRUML, Tomáš. Effect of pulsating water jet processing on erosion grooves and microstructure in the subsurface layer of 25CrMo4 (EA4T) steel. *Wear*. July 2023. Vol. 524–525, p. 204774. DOI 10.1016/j.wear.2023.204774.

28. AHMED, Aymen A., MHAEDE, Mansour, BASHA, M, WOLLMANN, Manfred and WAGNER, Lothar. The effect of shot peening parameters and hydroxyapatite coating on surface properties and corrosion behavior of medical grade AISI 316L stainless steel. *Surface and Coatings Technology*. October 2015. Vol. 280, p. 347–358. DOI 10.1016/j.surfcoat.2015.09.026.

29. WANG, Z.D., SUN, G.F., LU, Y., CHEN, M.Z., BI, K.D. and NI, Z.H. Microstructural characterization and mechanical behavior of ultrasonic impact peened and laser shock peened AISI 316L stainless steel. *Surface and Coatings Technology*. March 2020. Vol. 385, p. 125403. DOI 10.1016/j.surfcoat.2020.125403.

30. HONGCHAO, Qiao. Experimental investigation of laser peening on Ti17 titanium alloy for rotor blade applications. *Applied Surface Science*. October 2015. Vol. 351, p. 524–530. DOI 10.1016/j.apsusc.2015.05.098.

31. KUMAR, Dharmesh, NADEEM AKHTAR, Syed, KUMAR PATEL, Anup, RAMKUMAR, J. and BALANI, Kantesh. Tribological performance of laser peened Ti–6Al–4V. *Wear*. January 2015. Vol. 322–323, p. 203–217. DOI 10.1016/j.wear.2014.11.016.

32. STOLÁRIK, Gabriel, NAG, Akash, PETRŮ, Jana, SVOBODOVÁ, Jaroslava and HLOCH, Sergej. Ultrasonic Pulsating Water Jet Peening: Influence of Pressure and Pattern Strategy. *Materials*. 13 October 2021. Vol. 14, no. 20, p. 6019. DOI 10.3390/ma14206019.

33. NAG, Akash, SRIVASTAVA, Madhulika, PETRŮ, Jana, VÁŇOVÁ, Petra, SRIVASTAVA, Ashish Kumar and HLOCH, Sergej. Comparison of Continuous and Pulsating Water Jet during Piercing of Ductile Material. *Materials*. 6 May 2023. Vol. 16, no. 9, p. 3558. DOI 10.3390/ma16093558.

34. LEHOCKA, Dominika, KLICH, Jiri, BOTKO, Frantisek, SIMKULET, Vladimir, FOLDYNA, Josef, KREJCI, Lucie, STORKAN, Zdenek, KEPIC, Jan and HATALA, Michal. Comparison of ultrasonically enhanced pulsating water jet erosion efficiency on mechanical surface treatment on the surface of aluminum alloy and stainless steel. *The International Journal of Advanced Manufacturing Technology*. August 2019. Vol. 103, no. 5–8, p. 1647–1656. DOI 10.1007/s00170-019-03680-8.

35. Strengthening Effect after Disintegration of Stainless Steel Using Pulsating Water Jet. *Tehnicki vjesnik - Technical Gazette*. Online. August 2018. Vol. 25, no. 4. [Accessed 12 June 2023]. DOI 10.17559/TV-20170327134630.

36. SRIVASTAVA, Madhulika, HLOCH, Sergej, GUBELJAK, Nenad, MILKOVIC, Marijana, CHATTOPADHYAYA, Somnath and KLICH, Jiri. Surface integrity and residual stress analysis of pulsed water jet peened stainless steel surfaces. *Measurement*. September 2019. Vol. 143, p. 81–92. DOI 10.1016/j.measurement.2019.04.082.

37. SRIVASTAVA, Madhulika, HLOCH, Sergej, TRIPATHI, Rupam, KOZAK, Drazan, CHATTOPADHYAYA, Somnath, DIXIT, Amit Rai, FOLDYNA, Josef, HVIZDOS, Pavol, FIDES, Martin and ADAMCIK, Pavel. Ultrasonically generated pulsed water jet peening of austenitic stainless-steel surfaces. *Journal of Manufacturing Processes*. April 2018. Vol. 32, p. 455–468. DOI 10.1016/j.jmapro.2018.03.016.

38. MARRIOTT, J. B., ROWDEN, G., HAMMITT, F. G., THOMAS, G. P., WEBB, A. W. O., TABOR, D., FYALL, A. A., SMITH, A. and BRUNTON, J. H. The Erosion of a Cobalt-Chromium Alloy by Liquid Impact [and Discussion]. *Philosophical Transactions of the Royal Society of London. Series A, Mathematical and Physical Sciences*. 1966. Vol. 260, no. 1110, p. 144–152.

39. KAMKAR, N., BRIDIER, F., JEDRZEJOWSKI, P. and BOCHER, P. Water droplet impact erosion damage initiation in forged Ti–6Al–4V. *Wear*. January 2015. Vol. 322–323, p. 192–202. DOI 10.1016/j.wear.2014.10.020.

40. MA, Dina, MOSTAFA, Ahmad, KEVORKOV, Dmytro, JEDRZEJOWSKI, Pawel, PUGH, Martin and MEDRAJ, Mamoun. Water Impingement Erosion of Deep-Rolled Ti64. *Metals*. 18 August 2015. Vol. 5, no. 3, p. 1462–1486. DOI 10.3390/met5031462.

41. LIANG, X.Z., DODGE, M.F., JIANG, J. and DONG, H.B. Using transmission Kikuchi diffraction in a scanning electron microscope to quantify geometrically necessary dislocation density at the nanoscale. *Ultramicroscopy*. February 2019. Vol. 197, p. 39–45. DOI 10.1016/j.ultramic.2018.11.011.

42. ZRIBI, Zahra, KTARI, Hassan Houcin, HERBST, Frédéric, OPTASANU, Virgil and NJAH, Nabil. EBSD, XRD and SRS characterization of a casting Al-7wt%Si alloy processed by equal channel angular extrusion: Dislocation density evaluation. *Materials Characterization*. July 2019. Vol. 153, p. 190–198. DOI 10.1016/j.matchar.2019.04.044.

43. LANGFORD, Richard M. Focused ion beams techniques for nanomaterials characterization. *Microscopy Research and Technique*. July 2006. Vol. 69, no. 7, p. 538–549. DOI 10.1002/jemt.20324.